



Journal of the Egyptian Society for Basic Sciences-Physics (JESBSP)

<https://jesbsp.journals.ekb.eg/>

The Role of Frequency and Electromechanical Coupling on Electrical and Dielectric Properties for Barium Zirconate Titanate (BZT) Transducer.

M Mostafa^{*1}, Aseel M Altarawneh¹, Enas A Arrasheed^{1,2}, R Ghazy¹, O M Hemedat¹, A M A Henaish^{1,3}

¹ Physics Department, Faculty of Science, Tanta University, Tanta 31527, Egypt.

² Faculty of Science and Information Technology, Jadara University, Irbid, Jordan.

³ NANOTECH Center, Ural Federal University, Ekaterinburg 620002, Russia

* Corresponding author: maha_mostafa@science.tanta.edu.eg

Abstract

In the current study, a series of $BaZr_xTi_{1-x}O_3$ (BZT) was synthesized by tartrate precursor method, with ($x = 0.00, 0.15, 0.50, 0.75, \text{ and } 1$) that were then calcined and sintered for four hours at 1100°C . In order to describe the structural characteristics of prepared samples, X-ray Diffraction (XRD) is used. From the XRD pattern, the tetragonal phase was confirmed. Dielectric loss ($\tan\delta$) and the real and imaginary parts of the dielectric constant (ϵ' , ϵ'') were analyzed for their frequency dependency. The results show that at low frequencies, the values of ϵ' , ϵ'' and $\tan\delta$ have high values and rapidly decline with an increase in frequency. So BZT materials could have potential applications in the development of high-performance capacitors, resonators, filters, and sensors. The Nyquist plot shows two semicircles; the first one at higher frequency shows grain contribution and that at low frequency is grain boundary contribution. The decrease in a.c. resistivity with increasing temperature is observed at high temperature region indicating that the mobility of charge carriers is thermally activated which lead to the decrease of resistivity, so these materials may be suitable for high-temperature applications such as power electronics and electrical insulation. The sample $x = 0.75$ has high dielectric loss compared with other samples that assured by the a.c. resistivity whereas the sample $x = 0.75$ has the lowest resistivity. The coupling factor (K_p) is used to calculate the electromechanical behavior of a piezoelectric resonator which found to decrease by increasing Zr content from 0.64 to 0.92. The relationship between Zr content and the coupling factor (K_p) could also be useful for optimizing the composition of BZT materials for specific applications requiring high coupling.

Keywords: tartrate precursor method, Cole-Cole diagram, a.c resistivity, Dielectric loss, electric modulus, coupling factor.

Declarations The authors have no relevant financial or non-financial interests to disclose.

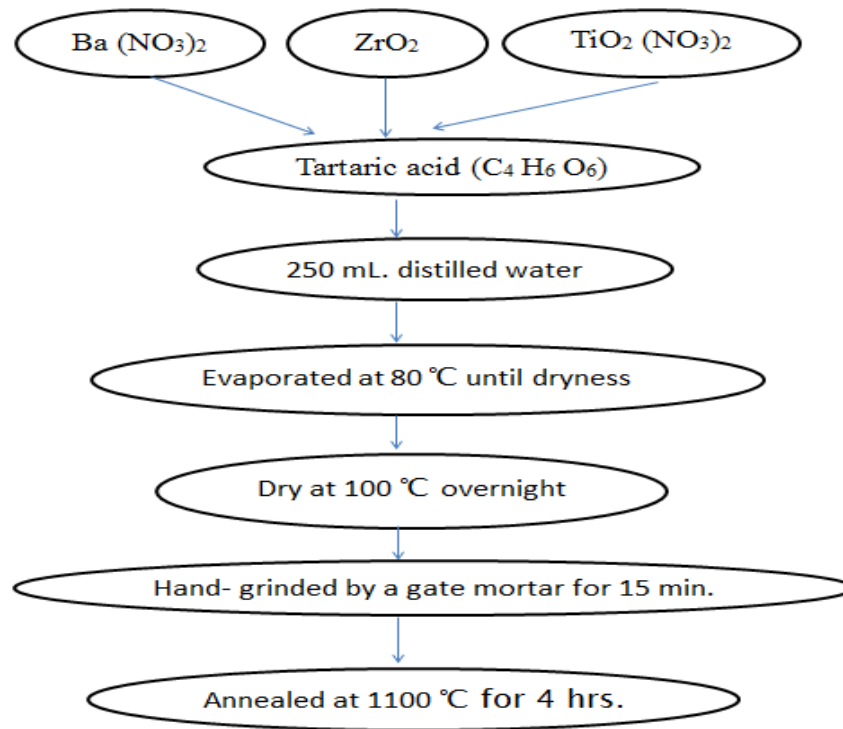
1. Introduction

In the recent times, the investigation of ferroelectric materials act a great scientifically and technologically interests in many applications such as resistive switching [1], catalysis [2], solar cells [3], electro-optic modulators [4], thermal imaging, PTC thermistor [5], capacitors [6,7], insulators, superconductors [8], parametric amplifiers [9], micro-electromechanical systems, energy harvesting and thermal sensors [10,11] due to significant physics of ferroelectric materials such as dielectric properties. Among these ferroelectric materials, BaTiO₃ (BT) is considered as the most promising piezoelectric materials which are used for many application such as, multilayer ceramic capacitors, piezoelectric transducer device, piezoelectric memories, pyroelectric sensors for security systems, cell phones, and piezoelectric transducers [12–14]. Various procedures developed to synthesize BT were reported in the literature, including electrophoretic precursor technique, deposition, sol-gel, hydrothermal synthesis, molecular composite hydroxide mediated and tartrate precursor method [15–20]. The characteristics of BT can be efficiently controlled by doping or substituting with different elements. Barium zirconium titanate, Ba(Zr_xTi_{1-x})O₃ (BZT) is one of attractive candidates with great potential as piezoelectric energy harvester. Generally, the substitution of Zr elements into B-sites of BaTiO₃ perovskite structure induced the lattice distortions and promotes a morphotropic phase boundary which is critical for the dielectric and piezoelectric properties improvement. However, the nature of phase transitions in morphotropic phase boundary region is greatly influence by Zr content. This is because the Zr⁴⁺ ions are chemically more stable than Ti⁴⁺ ions and thus offer greater stability of the BaTiO₃ perovskite unit cell [21-23]. The Zr⁴⁺ substitution at Ti-site has been found to be an effective way to decrease the Curie temperature and to exhibit several interesting features in the dielectric behavior of BZT ceramics [24]. Barium zirconate is one of the widely investigated perovskites oxides. The current work aims to prepare BaZr_xTi_{1-x}O₃ (x = 0, 0.15, 0.5, 0.75, and 1) nanopowders using tartrate precursor technique and studying the impact of the Zr⁴⁺ substitution ratio on the morphology, structure, coupling factor, and ferroelectric characteristics of BZT was examined.

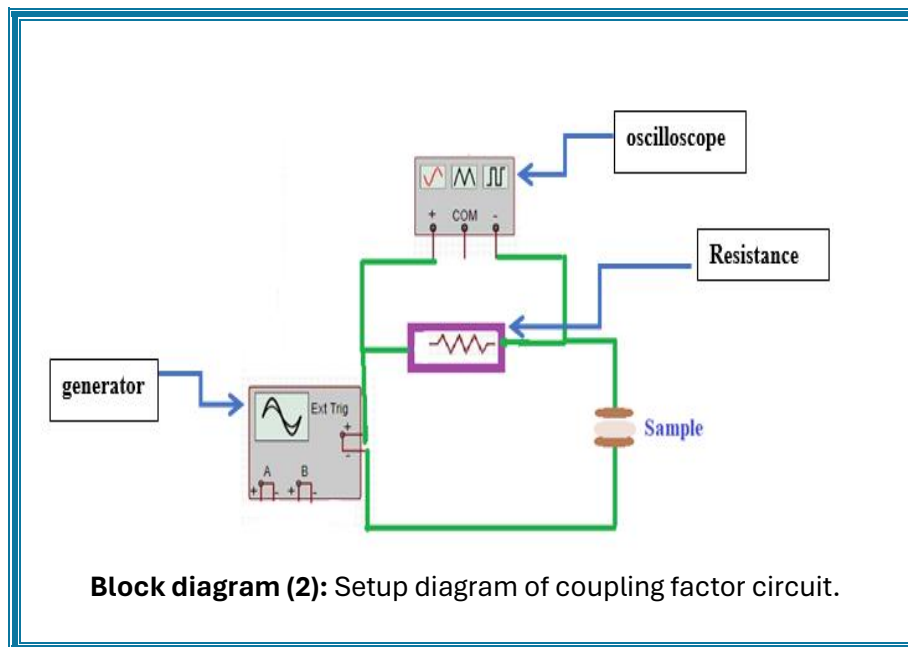
2. Materials and Methods

BaZr_xTi_{1-x}O₃ (BZT) where (x = 0, 0.15, 0.5, 0.75 and 1) were prepared by the tartrate precursor method as shown in **block diagram (1)**. The samples were examined by the XRD technique with a Philips model PW-1729 diffractometer (Cu-K α radiation source with $\lambda = 1.540598 \text{ \AA}$) in the 2θ range from 20 to 80°. The Alpha Analyzer measures (Novo control GmbH) used to determine the complex dielectric, modulus, conductivity, and impedance function of materials independence of frequency with high precision. The frequency-dependent electrical and dielectric properties of the BZT tablets were recorded by a high-precision LCR meter bridge (HP-6284A). Using RLC bridge of type (BM591), dielectric properties as a function of temperature at different frequencies were measured. EIS Spectrum Analyzer Version 1.0 software is employed to adjust these Nyquist plots for BZT sample. The coupling factor K_p was estimated from the resonance

f_r and anti-resonance frequency f_a of disk of the prepared samples which acting as piezoelectric resonator vibrating in longitudinal mode as shown in **block diagram (2)**.



Block diagram (1): Samples preparation via the tartrate precursor method.

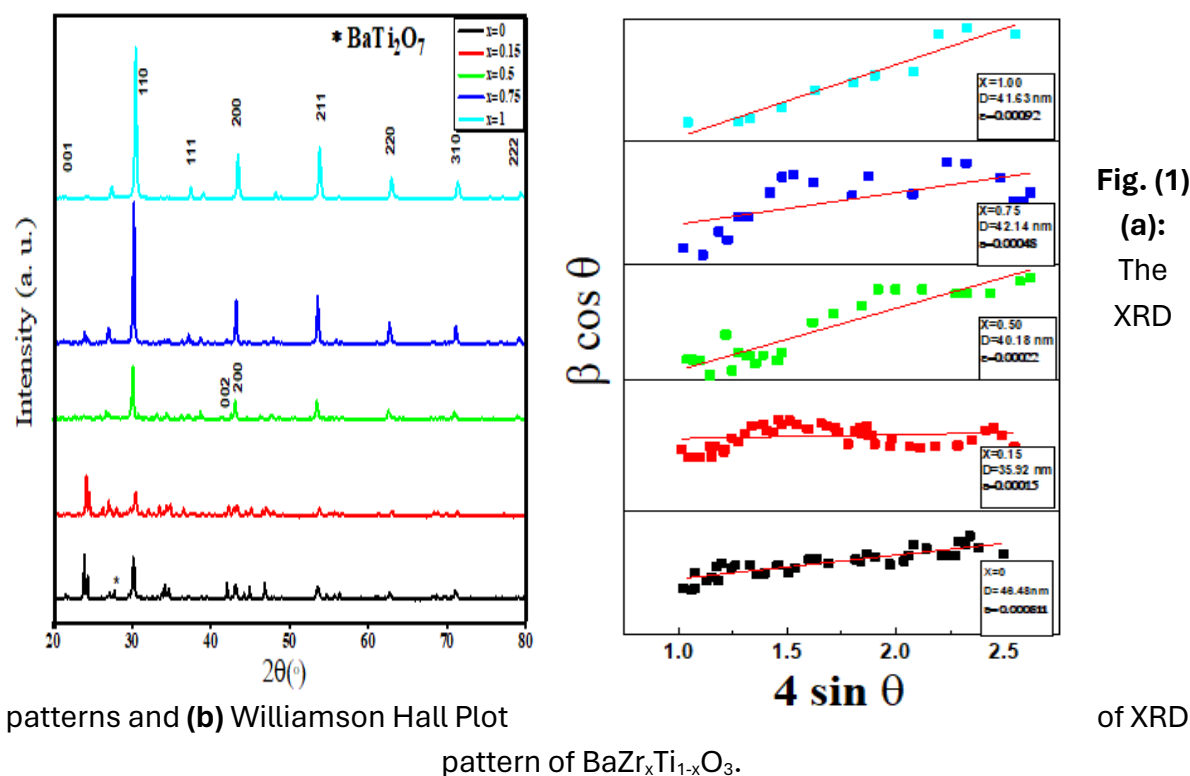


Block diagram (2): Setup diagram of coupling factor circuit.

3. Results and Discussion

3.1. X-Ray Analysis

Fig.(1a) displays XRD patterns of BZT samples that indicated the existence of tetragonal phase with space group (p4mm) [25]. The tetragonal structure diffraction peaks are (001), (110), (111), (200), (210), (211), (220), (310), and (222) at $2\theta = (21.2^\circ, 30.10^\circ, 37.1^\circ, 43.1^\circ, 48.5^\circ, 53.5^\circ, 62.6^\circ, 71^\circ, 75^\circ, 79^\circ)$ respectively. The pattern's sharp and defined peaks elucidate a high degree of crystallinity, and the intensity of the main peak (110) increases as Zr content raises. The presence of tetragonal phase is assured by the splitting of two diffraction peaks (002) at $2\theta = 42.74^\circ$ and (200) at $2\theta = 43.25^\circ$ up to $x=0.75$ Zr content, whereas the sample $x=1$ no splitting elucidates the cubic phase. The existence of a weak peak at $2\theta = 27.74^\circ$ is owing to the existence of a small amount of $BaTi_2O_7$ [26], the amount of which decreases as the Zr content raises. Similar results have also been reported indicating the smaller amount of $BaTi_2O_7$ in ferroelectrics [26]. The average crystallite size (D) of the perovskite structure is calculated using Scherer's equation [27]. It is noted that D of the BZT cubic phase dropped for $x=1$ and grew with increasing Zr concentration up to $x=0.75$ as shown in **Fig. (2)**



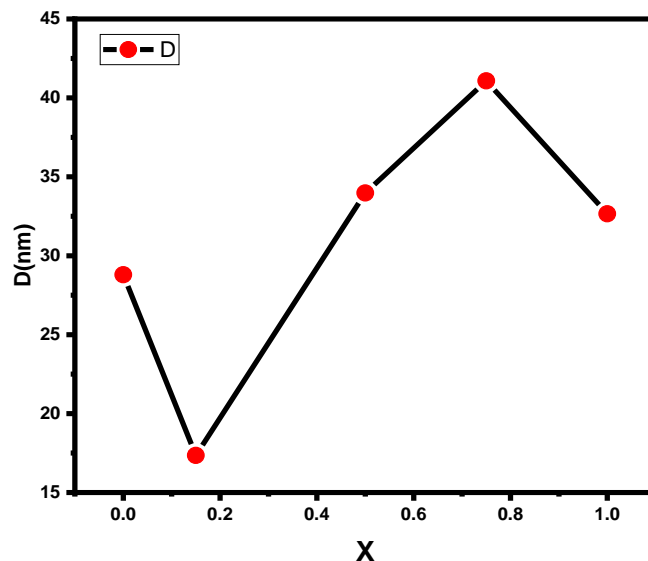


Fig. (2): Crystallite size of $\text{BaZr}_x\text{Ti}_{1-x}\text{O}_3$ for different Zr content.

X-ray diffraction patterns are influenced by the size of crystallites and lattice strain. W–H analysis is used to distinguish the crystallite size- and strain-induced deformation peak considering the broadening of the peak width as a function of 2θ . The total broadening, β , of the peaks is due to the combine effect of broadening due to crystallites size, β_D , and broadening due to strain, β_ε . Therefore the total broadening is given by[25]

$$\beta = \beta_D + \beta_\varepsilon = \frac{k\lambda}{D \cos\theta} + \frac{4 \varepsilon \sin \theta}{\cos \theta} \quad (1)$$

where β is the full width at half maximum (FWHM) of a radiant peak, k is the shape factor ($k = 0.89$), λ is the X-ray wavelength (1.54056 \AA), θ is the diffraction angle of Bragg, D is the crystallite size (nm), and ε is the microstrain.

Rearranging Eq. (1) gives

$$\beta \cos\theta = 4 \varepsilon \sin \theta + \frac{k\lambda}{D} \quad (2)$$

From **Fig.(1b)**, W-H plot, the average size of the crystallites and the strain can be estimated by the Y-intercept extrapolation and the slope of the line

$$D = \frac{K \lambda}{Y_{\text{Intercept}}} \quad (3)$$

$$\varepsilon = \text{slope} \quad (4)$$

The relation between $\beta \cos\theta$ and $4 \sin \theta$ was fitted to straight line with correlation coefficient value of R^2 is 0.92. The intrinsic strain is represented by the slope of this straight line, and the average particle size of the $\text{BaZr}_x\text{Ti}_{1-x}\text{O}_3$ nanocrystals is yielded from the Y intercept. The lattice strain is attributed to the lattice volume changes, either expansion or contraction, restricted by the quantum size confinement controlling the

nanocrystals. Hence, the atomic arrangement will be slightly modified, compared to their bulk. Also, due to the size confinement, many defects will be created at the lattice structure, which result in the lattice strain. As calculated from W-H model, the average crystallite size was in the range (35–46) nm, which is significantly less than the size estimated using Debye-Scherrer formula due to the term of intrinsic strain added to Debye-Scherrer formula to get W-H model.

3.2. FTIR spectra:

The absorbance spectra of FTIR $\text{BaZr}_x\text{Ti}_{1-x}\text{O}_3$ are shown in **Fig. 3** within the range of 200–4000 cm^{-1} . The FTIR spectra showed two principal vibrational absorption bands around 350 cm^{-1} and 548 cm^{-1} ; other additional peaks appear at 3394 cm^{-1} due to the existence of O–H vibration of water adsorption by the sample, which has an asymmetric stretching mode which increases by increasing Zr content. Tartaric acid interacts with BaTiO_3 during production, as evidenced by a peak at 1428 cm^{-1} , which is attributed to an asymmetric vibration of the C–O bond [26]. The first two absorption bands are associated with stretching and bending vibrational modes in Ti–O. Absorption bands between 400 and 600 cm^{-1} are often linked to the initiation of Zr–O and Ti–O stretching vibrations [27]. The peak at around 1143 cm^{-1} is attributed to the symmetrical CO_2 and CH_2 twisting mode. The absorption bands at 2464 cm^{-1} and 2927 cm^{-1} are related to the asymmetric and symmetric C–H stretching vibrations of the CH_2 and CH_3 groups, respectively [28]. C–O deformation vibration peaks are around 1428 cm^{-1} and 1168 cm^{-1} . The C–C stretching vibration is linked to the absorption band at 859 cm^{-1} . The peaks at 1762 cm^{-1} (C=O stretching vibration), 1438 cm^{-1} (C–O asymmetric stretching vibration), 859 cm^{-1} and 693 cm^{-1} (C=O bending vibration) all belong to the BaCO_3 phase [29]. As x increases from 0 to 0.75, the frequency of the absorption band at 691 cm^{-1} increases before dropping again. The initial absorption band, at 480 cm^{-1} , has the same pattern of activity. By increasing the Zr content, shoulder $\cong 600 \text{ cm}^{-1}$, we may explain this behavior to a modification in the bond length [30].

In conclusion, XRD analysis and the FT-IR spectra are consistent, demonstrating that the formation temperature of perovskite BZT powder is more than or equal to 1100 °C depending on the percentage of the Zr content in the prepared sample.

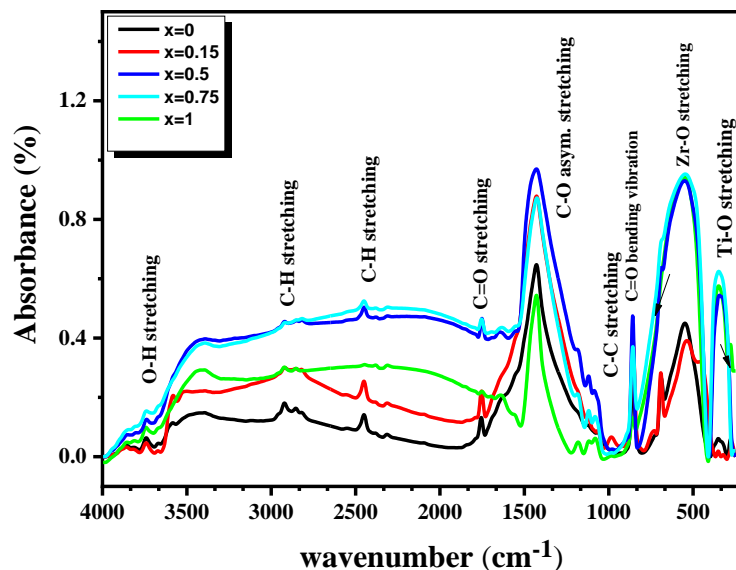


Fig. (3): The FTIR absorbance spectra for $\text{BaZr}_x\text{Ti}_{1-x}\text{O}_3$ samples.

3.3. SEM Micrographs

Fig. 4. shows the Scanning Electron Microscopy (SEM) images of $\text{BaZr}_x\text{Ti}_{1-x}\text{O}_3$. SEM images of $\text{BaZr}_x\text{Ti}_{1-x}\text{O}_3$ showed the crystalline nature of the prepared nanoparticles and provide such a type of agglomeration. The presence of Zr ions increases the grain size, as seen by a correlation between grain size and Zr concentration. The grain sizes of the nanoparticles were found to be in the range of 1.54–2.80 μm and listed in **Table (1)**. Therefore, the presence of Zr concentration improves densification during sample preparation. Due to the fact that the average grain size calculated from the SEM micrograph is greater than the crystallite size calculated using Scherer's equation from X-ray analysis, the grain is assumed to be occupancy of crystallites.

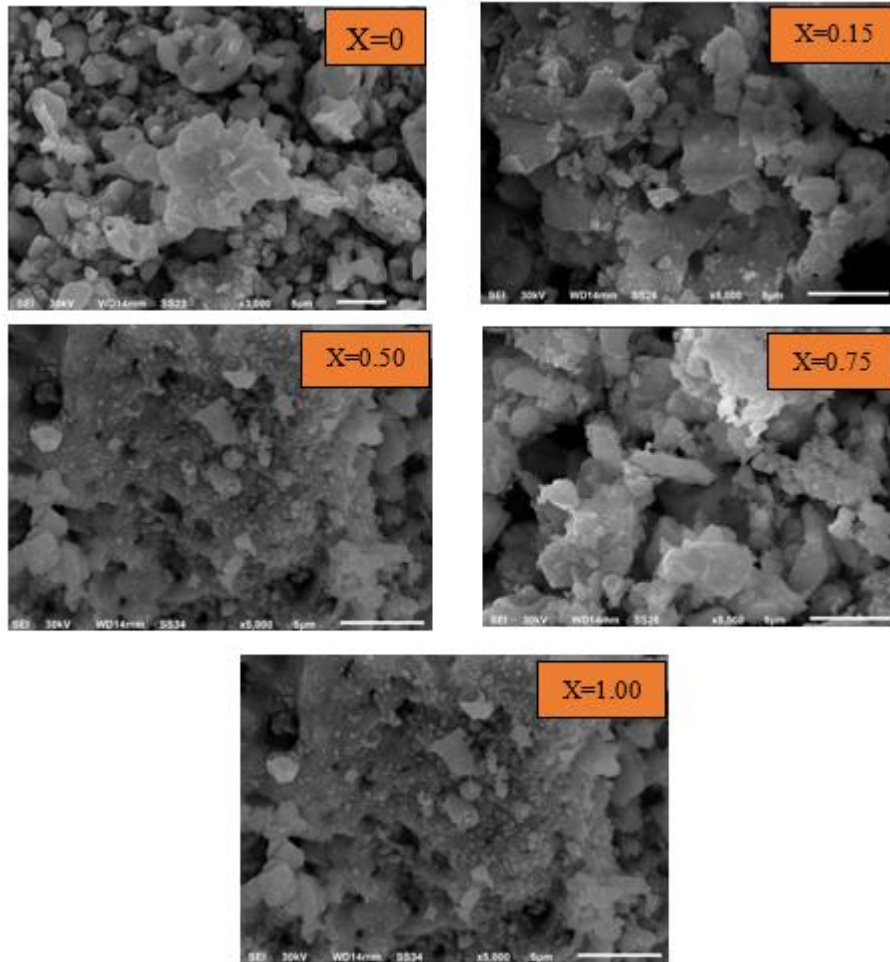


Fig. (4): SEM micrograph of $BaZr_xTi_{1-x}O_3$.

Table (1): Crystallite sizes, Particle sizes and Grain sizes for $BaZr_xTi_{1-x}O_3$.

X	XRD		SEM
	Scherer formula	Williamson–Hall method	grain sizes (μm)

	D(nm)	D(nm)	$\epsilon \times 10^{-3}$	
0.0	28.80	46.68	0.811	1.54
0.15	17.35	35.92	0.157	1.73
0.5	33.98	40.18	0.227	1.78
0.75	41.08	42.14	0.484	2.08
1.0	32.66	41.63	0.9279	2.80

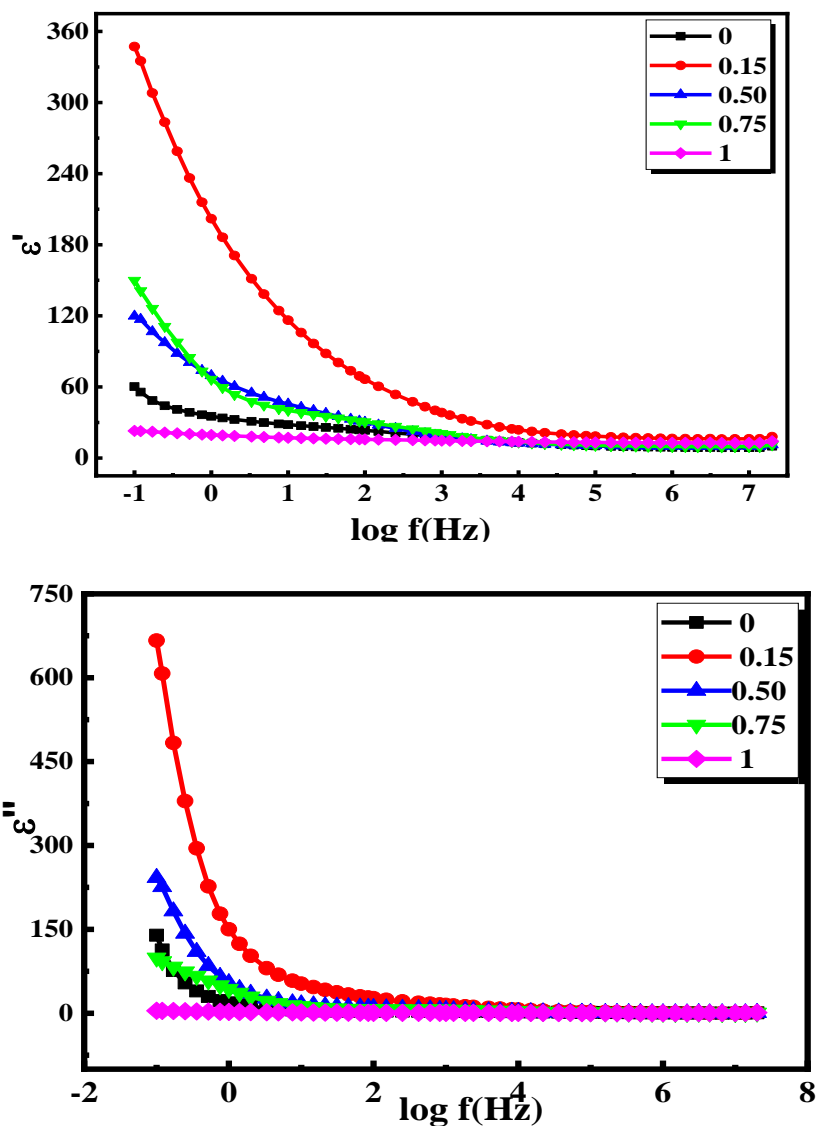
3.4. Frequency dependence of dielectric properties:

Fig. (5) displays the variation of real and imaginary part of dielectric constant (ϵ' , ϵ'') and dielectric loss ($\tan\delta$) as a function of frequency in the range from (10^{-1} Hz - 2×10^7 Hz) at room temperature. At low frequency the values of ϵ' , ϵ'' and $\tan\delta$ have high values and rapidly decrease with the increase of temperature while they are very low and reach near zero at high frequency and become nearly independent on frequency [28]. It may be owing to the effect of defects with opposite charge that leads to the charges (dipoles) preserve neutrality, and the decrease of polarization [29]. At high frequency these dipoles can't follow the external electric field causes the dielectric constant decreases. The dielectric loss is considered as a combination between electrical conduction and the orientation polarization. So we can consider the energy loss occurs due to the DC conductivity and dipole relaxation [30]. The dielectric loss has a relaxation process around 2.4×10^3 Hz. The calculated corresponding relaxation time is tabulated in **Table (2)**

Table (2): Permittivity and relaxation time for different Zr content.

X	At frequency (10^3 Hz)		Relaxation time ($\tau_c * 10^{-3}$)	
	ϵ'	ϵ''	$\tau_{\tan\delta}$	$\tau_{\epsilon''}$
0.0	17.95	3.50	8.87	45
0.15	38.35	14.90	4.15	10
0.50	18.41	6.11	8.64	26
0.75	20.75	6.30	7.67	25
1.0	14.70	0.69	10	11

Fig. (6) shows the real and imaginary part of electric modulus M' , M'' respectively as a function of frequency and Cole-Cole diagram (M' vs. M'') for BZT with $x= (0 - 1)$. The Cole -Cole plot shows two semicircles for Zr contents lies between (0 - 0.75) and deformat at high Zr content =1. The first semicircles at higher frequency shows grain contribution and that at low frequency sites is grain boundary contribution. With the increase of Zr contents the peaks of the semicircle at high frequency shifted to low frequency. The two semicircles have different radii and different intensity which are attributed to the different values of the resistance and capacity for grain and grain boundary.



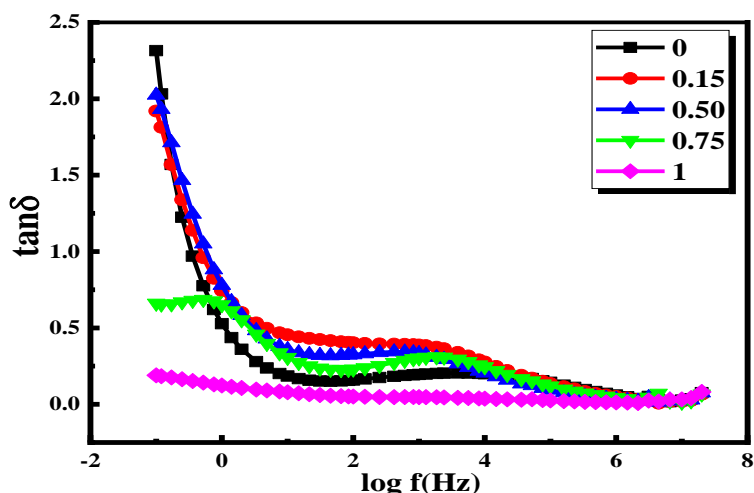


Fig. (5): Frequency dependence of real and imaginary part of dielectric constant ϵ' , ϵ'' respectively and dielectric loss ($\tan\delta$) for different Zr content.

The Nyquist plots of BZT samples over a wide frequency range ($0.1 - 2 \times 10^7$ Hz) are presented in **Fig. (6)**. The Nyquist plots are consistent with more than one semicircle proving the existence of more than one contribution. EIS Spectrum Analyzer Version 1.0 software is employed to adjust these Nyquist plots for BZT sample. These semicircles clustered together indicate that the BZT samples show non-Debye behavior due to the distribution of relaxation times in the samples. For $x=0$, the semicircles are oriented towards the real impedance axis with more convex shapes, due to the higher conductivity of this sample. The adequate electrical circuit consists of series combination of two resistors R_2 and R_3 , where each one is in parallel with two capacitors (C_1 and CPE_1) due to the grain contributions of the sample at higher frequency side and grain boundary contribution at lower frequency side. On the other hand, the electrode effects are insignificant, i.e., R_1 is very small compared with R_2 and R_3 . The fitting of this data gives the values of resistance and capacitance for non-ideal capacitance, CPE, are tabulated in **Table (3)**. This non-ideal behavior can be correlated with several factors, such as grain orientation, grain boundary, and defects in the structure. With the increase of Zr content, the value of grain resistance R_2 increased from 0.001 to 3900 ($G\Omega/cm^2$) and the value of grain boundary resistance R_3 increased from 42 to 8980 ($G\Omega/cm^2$). The value of grain capacitance C_1 varying from 10 to 340 (nF/cm^2). The values of grain boundary capacitance P_1 varying from 0.168 to 7.99 (PF/cm^2).

Table (3): Koop parameters of grain and grain boundaries for different Zr content.

Zr content (x)	C_1 (nF/cm^2)	R_1 (Ω/cm^2)	R_2 ($G\Omega/cm^2$)	R_3 ($G\Omega/cm^2$)	P_1 (PF/cm^2)
0.00	342	200.95	0.001	42.5	0.168
0.15	34.2	116.64	3.85	7.97	0.980
0.50	9.85	229.72	65.5	96.8	0.257
0.75	88.3	195.61	37.2	73	0.357
1.00	168	192.09	3900	8980	7.97

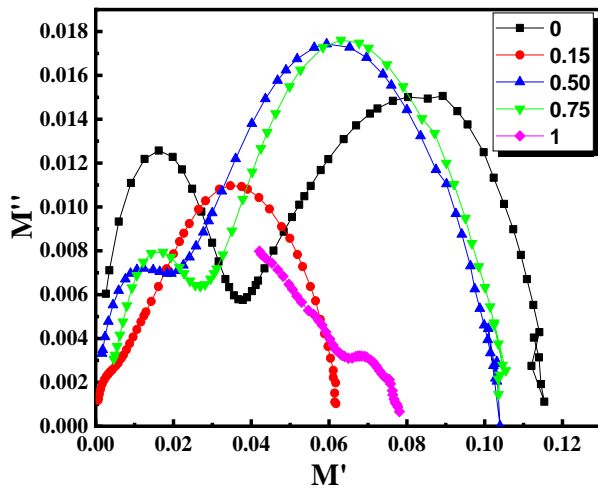
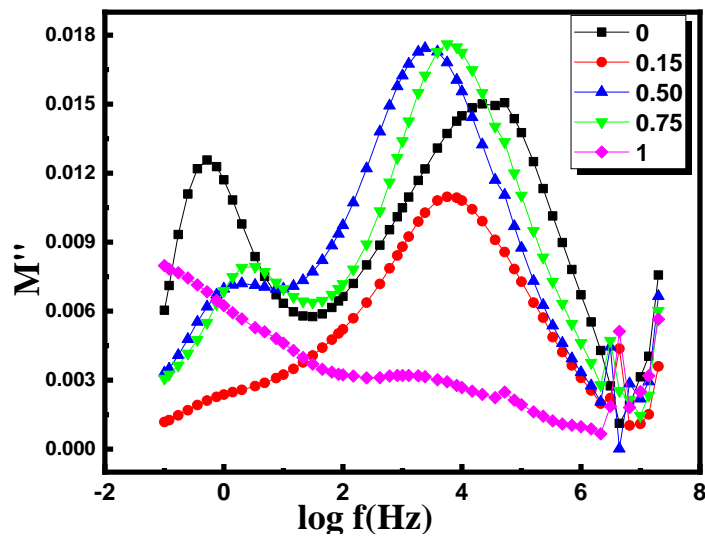
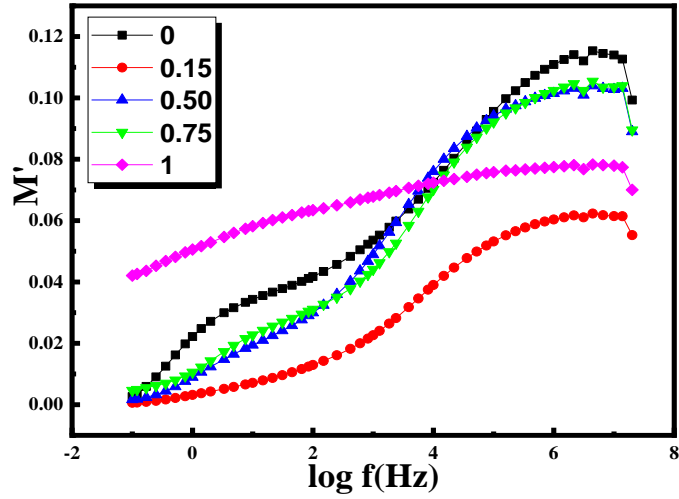


Fig. (6): real and imaginary part of electric modulus M' , M'' respectively as a function of frequency and Cole-Cole diagram (M' vs. M'') for different Zr content.

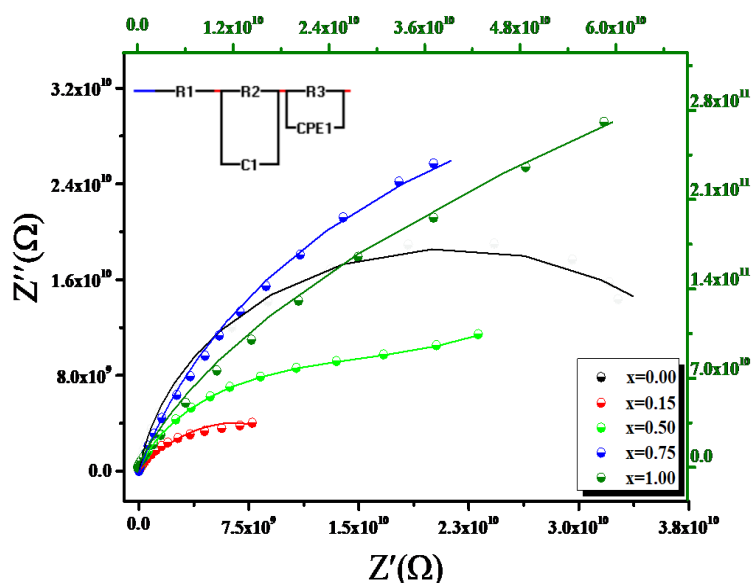


Fig. (7): Z'' vs Z' for different Zr content.

3.5. Temperature dependence of Electrical and Dielectric properties:

3.5. a. Ac conductivity:

The a.c. resistivity of $BaZr_xTi_{1-x}O_3$ as a function of reciprocal temperature is shown in **Fig. (8)** at frequencies of 10 kHz, 50 kHz, and 100 kHz. As the frequency increases, the resistivity decreases; this could be due to the high relaxation time of charge carriers at low frequencies, resulting in high resistivity; additionally, as the frequency increases, more charge carriers can respond easily to the external electric field, resulting in lower resistivity. At high temperatures, a decrease in a.c. resistivity with increasing temperature is observed, indicating that the mobility of charge carriers is thermally activated, resulting in a decrease in resistivity. When an electric field is applied to our samples, the hopping electron between Ti^{3+} and Ti^{4+} causes conduction. The decrease in ac resistivity with increasing temperature indicated a negative coefficient of resistance for the material. As shown in **Table (4)**, the behavior of $\ln\rho$ vs. Zr content follows the same pattern as the variation of porosity vs. Zr content. The total a.c. resistivity can be given from the equation:

$$\rho_{AC} = \rho_{DC} + A \omega^n \quad (5)$$

where A is a constant and the exponent n is the frequency constant. **Fig. (10)** depicts the calculated values of n . The value of n decreases with increasing frequency and also with increasing Zr content, with $x = 0.75$ having the lowest value. When the Zr content increases, the samples become more frequency dependent and sensitive to any frequency variation.

Table (4): The values of porosity, crystallite size and $\ln\rho$ for different Zr content.

x	porosity	Crystallite size (nm)	$\ln\rho$ at 100 kHz
0	0.41	28.80	12.94
0.15	0.43	17.35	13.07
0.50	0.47	33.98	13.14
0.75	0.50	41.08	13.25
1	0.52	32.66	13.34

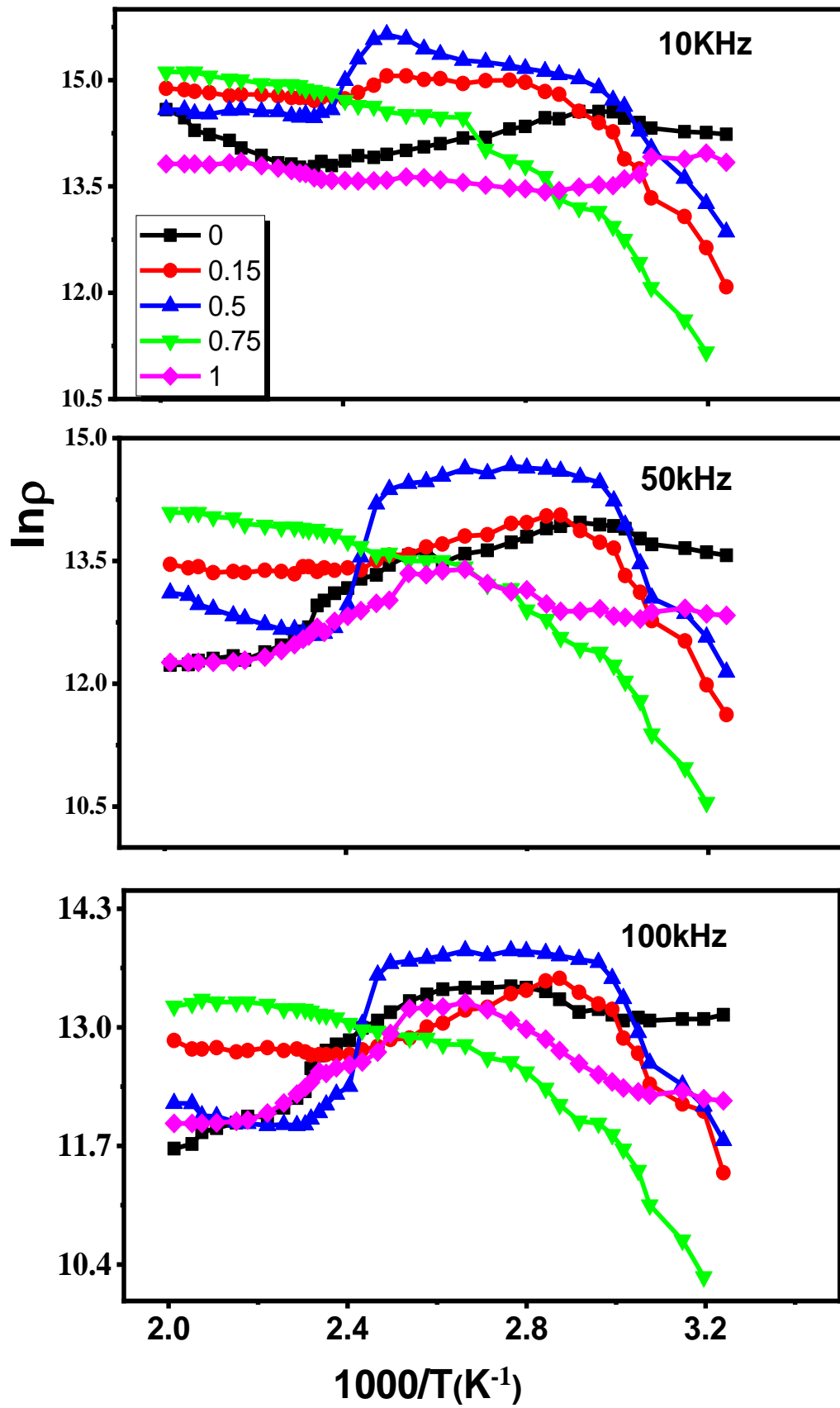


Fig. (8): $\ln p$ vs. $1000/T(K)$ for BZT samples at different Zr content at 10 kHz , 50kHz and 100kHz.

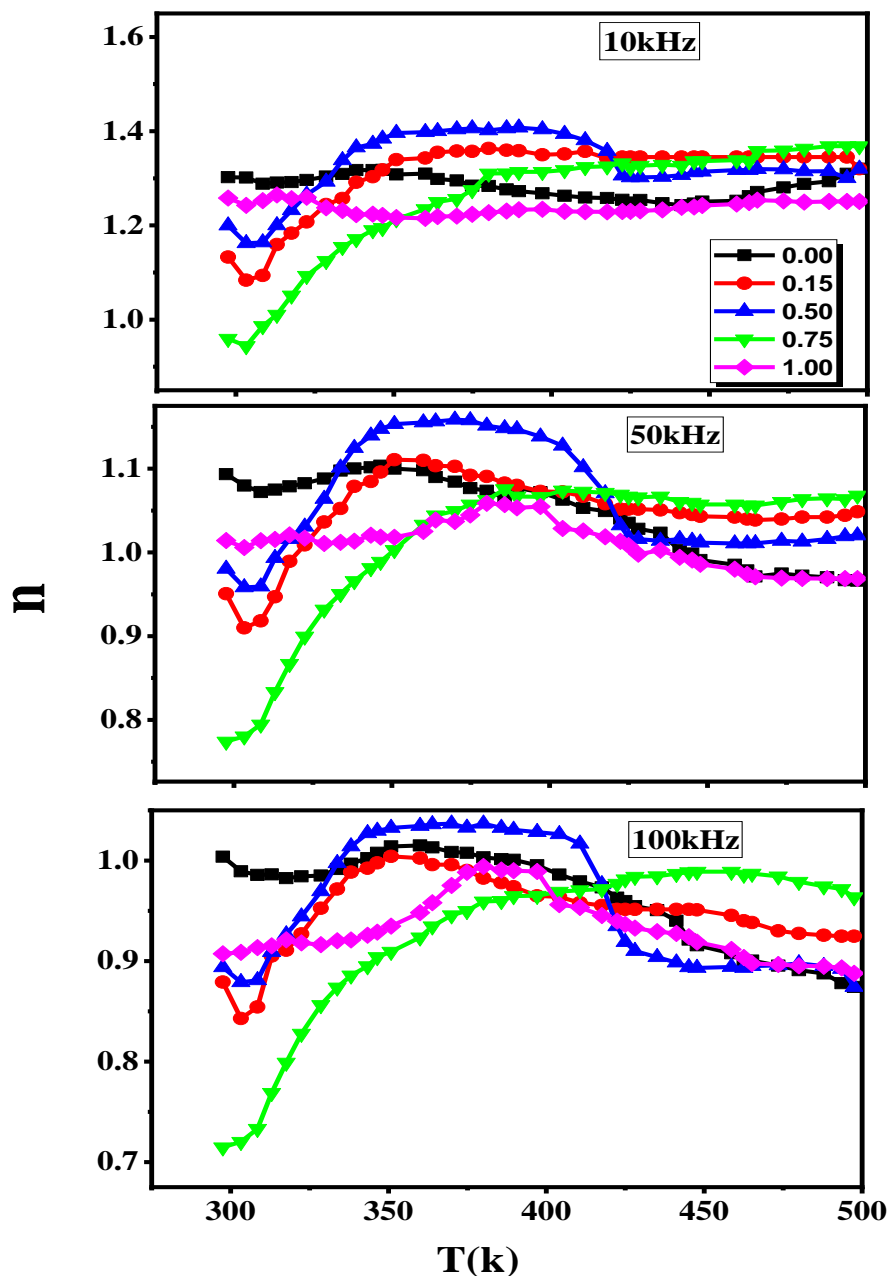


Fig. (9): The variation of n with temperature T (K) at various frequencies of BZT samples at different Zr content.

3.5.b. Temperature dependence of dielectric constant:

The temperature dependence of dielectric constant at three fixed frequencies 10 kHz, 50 kHz and 100 kHz for BZT samples are shown in **Fig. (10)**. It is evidence that the dielectric constant decrease with increasing frequency, this may be due to the effects of space charge polarization or Maxwell-Wagner type interfacial polarization [31]. The dielectric constant exhibits a peak around room temperature and then decrease with farther

increase temperature. This peak which corresponds to the Curie point to the transition from ferroelectric to paraelectric phase and originated from the presence of the BaTi₂O₇ phase. This phase appears in the XRD patterns which confirm our discussion. From **Fig.(10)** it is seen that the maximum dielectric constant is observed for $x = 0.75$ composition at different frequencies, which may be due to the dense microstructure and the possible induced strain by Zr⁴⁺ in BaTiO₃ lattice [24].The maximum value of dielectric constant corresponds to Curie temperature [32].As the temperature rises, the mobility of charge carriers increases, increasing conductivity and polarization of the samples and, as a result, raising the dielectric constant. Except for $x = 0.75$, the dielectric constant is nearly independent of temperature for all samples. The Curie temperature varies significantly with Zr content and reaches a maximum at $x= 0.75$, as shown in **Table (5)**. The behavior of the material near the phase transition is related to the correlation between the maximum value of the dielectric constant and the Curie temperature. The dielectric constant of the material increases as the temperature approaches the Curie temperature due to increased polarization fluctuations. The material undergoes a phase transition at the Curie temperature, and the dielectric constant reaches its maximum value before decreasing as the temperature rises further. As a result, the maximum value of the dielectric constant is typically observed near the Curie temperature. By measuring the dielectric constant as a function of temperature, one can determine the temperature at which the dielectric constant has the greatest value, which corresponds to the material's Curie temperature. This data can be used to better understand the material's electrical properties and potential applications in electronic devices. The dielectric constant for the cubic phase decreases at $x = 1$. We can conclude that the dielectric properties of the samples are affected by the method of preparation, and some variation in dielectric constant values is to be expected.

Table (5): Curie temperature and dielectric constant for different Zr content.

x	T _c (K)	Dielectric constant at (50 kHz)
0	343	5.87
0.15	348	10.91
0.5	368	11.66
0.75	370	21.43

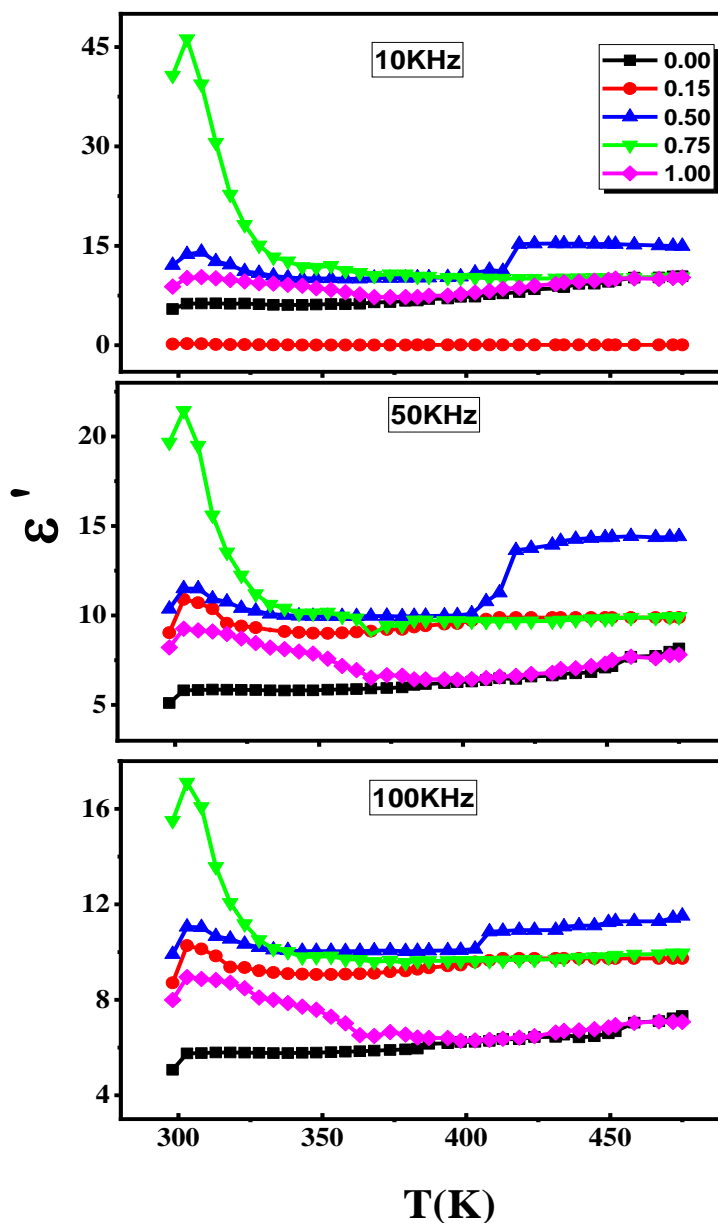


Fig. (10): The variation of dielectric constant as a function of T (K) for BZT samples.

3.5c Temperature dependence of dielectric loss:

The dielectric loss ($\tan(\delta)$) for all samples at different frequencies (10kHz, 50kHz, and 100kHz) is shown in **Fig. (11)**. As shown in **Fig. (10)**, $\tan(\delta)$ behaves similarly to dielectric constant. When compared to other samples, sample $x = 0.75$ has a high dielectric loss. These results are correlated by AC resistivity, with sample $x = 0.75$ having the lowest resistivity as shown in **Table (6)**. For all samples, increasing frequency reduces $\tan(\delta)$.

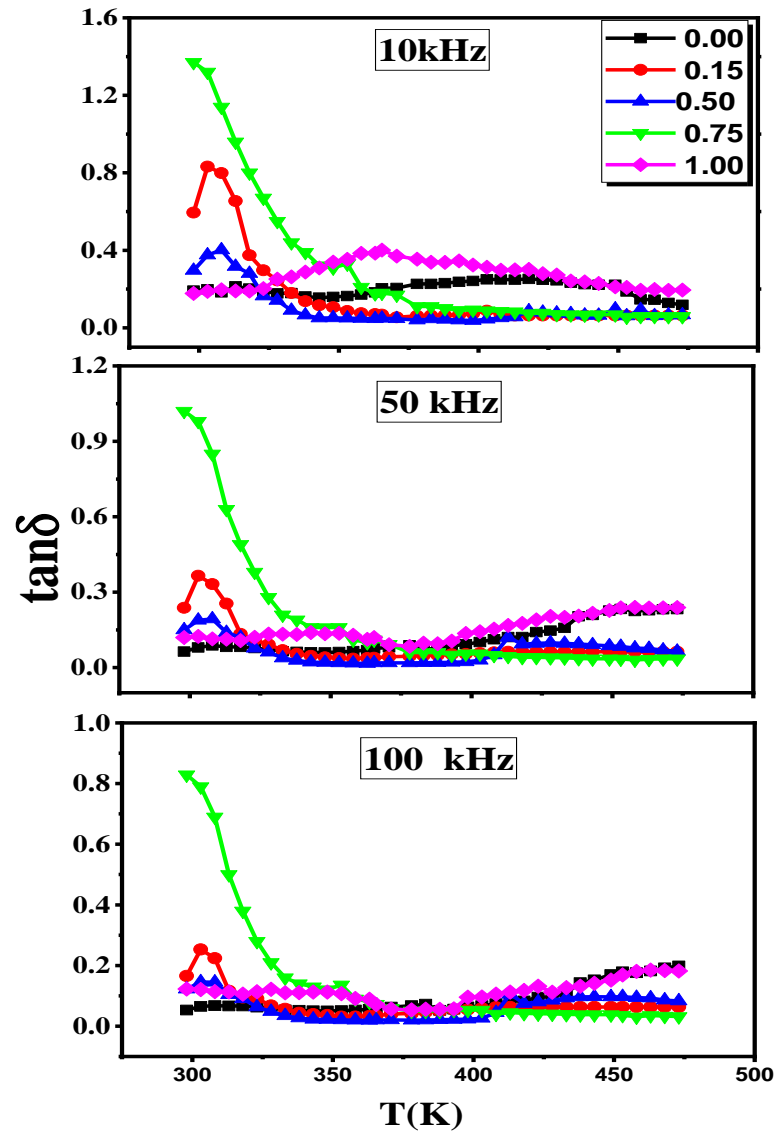


Fig. (11): $\tan(\delta)$ as a function of T (K) for different Zr content.

Table (6): Curie temperature, dielectric loss, and resistivity at 100 kHz for different Zr content.

x	T_c (K)	$\tan\delta$ at 100 kHz	ρ ($\Omega.m$) at 100 kHz
0	373	0.17	585034.1
0.15	348	0.25	648989.9
0.5	368	0.14	1025721
0.75	363	0.83	97015.17
1	383	0.12	553534.6

3.6 Effect of Zr contents on the coupling factor K_p :

The coupling factor (K_p) is used to calculate the electromechanical behavior of a piezoelectric resonator. It is defined as the square root of the ratio of mechanical energy available to total input electric energy. Coupling factor can measure the resonance (f_r) and antiresonance (f_a) frequencies of a sample that is vibrating in longitudinal mode as a piezoelectric resonator [33]. The equation yields the longitudinal mode coupling factor (k_p) [34].

$$K_p = \sqrt{2.51 \frac{(f_a - f_r)}{f_r}} \quad (6)$$

Where f_a and f_r represent the anti-resonance and resonance frequencies, respectively.

The ultrasonic wave velocity C is estimated from the relation: -

$$f_r = \frac{C}{2\pi r} \quad (7)$$

where C is the wave velocity and r is the radius of the tablet (0.36 cm). **Fig. (12)** depicts the coupling factor k_p as a function of ZrO_2 content for samples. It was discovered that increasing the Zr content from 0.64 to 0.92 decreased the coupling factor; the doping processes are a mechanism for introducing vacancies, which facilitate domain wall motion. At very low electric field and mechanical stress levels the domain wall motion can be displaced, allowing it to vibrate more easily [35]. These effects help the polarized tables vibrate at a lower frequency, which leads to an increase in the K_p . The value of K_p for pure samples $x=0$ ($BaTiO_3$) is higher than for all samples with Zr content, which is attributed to the sample's decreased tetragonality. The effect of ZrO_2 in the Ultrasonic velocity of polarized disc is shown in **Fig. (13)**. The ultrasonic waves are affected by the concentration of vacancies created by ZrO_2 doping. Because of the tetragonality of the sample and the occupation of all vacancies by Zr^{4+} ions, these vacancies help to lower the resonance frequency, which causes the ultrasonic wave velocity to decrease up to $x=0.5$ and then increase again, as shown in **Table (7)**.

Table (7) compares the published data to our current data in terms of K_p . According to the table, our nano composite $BaZr_xTi_{1-x}O_3$ has a high quality for electromechanical K_p in technological applications.

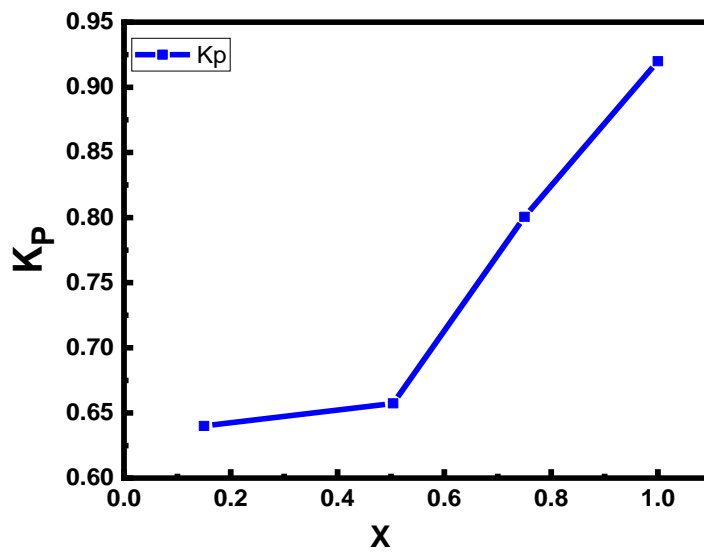


Fig. (12): The effect of Zr content (x) on the coupling factor (K_p).

Table (7): K_p and T_c of the published data and our present data and the ultrasonic velocity (C) for different Zr content.

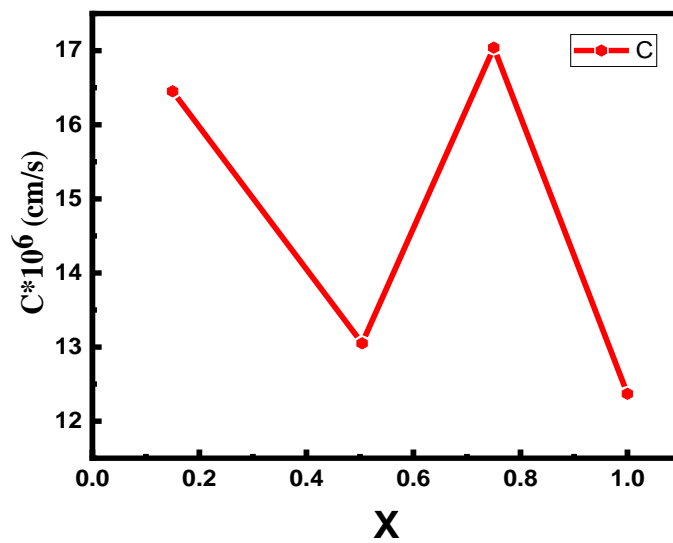


Fig. (13): The effect of Zr content (x) on the ultrasonic velocity.

4. Conclusions

In

sample	dopant	T _c (°C)	K _p	Reference	C*10 ⁶ (cm/s)
BaTiO ₃	Li	130	0.4	[36]	
BaTiO ₃	LiF	73	0.5	[37]	
Ba(Zr _{0.10} Ti _{0.90})O ₃	Zr	82.7	0.29	[38]	
Ba _{0.85} TiO ₃	Ca	130	0.21	[39]	
BT	-	91	0.35	[40]	
BZT	BCT	-	0.50	[41]	
BZT		89.3	0.42	[42]	
BaTiO ₃	-	155	0.93	Present work	18.61
BaZr _{0.15} Ti _{0.85} O ₃	Zr	130	0.64	Present work	16.45
BaZr _{0.50} Ti _{0.50} O ₃	Zr	70	0.80	Present work	13.05
BaZr _{0.75} Ti _{0.25} O ₃	Zr	140	0.67	Present work	17.04
BaZrO ₃	Zr	110	0.92	Present work	12.37

summary, BaZr_xTi_{1-x}O₃, with (x = 0.00, 0.15, 0.50, 0.75, and 1) ferroelectric nanoparticles are successfully synthesized via the tartrate precursor method. This paper is applying XRD, real and imaginary part of dielectric constant and dielectric loss as a function of frequency, Cole – Cole plot, Ac conductivity, temperature dependence of dielectric properties and Coupling factor measurements respectively. The presence of tetragonal phase is assured by the splitting of two diffraction peaks (002) at $2\theta = 42.74^\circ$ and (200) at $2\theta = 43.25^\circ$ up to x=0.75 Zr content. The dielectric loss has a relaxation process around 2.4×10^3 Hz. The decrease in ac resistivity with increasing temperature at higher temperature indicated that the material has negative coefficient of resistance of conductivity. The Curie temperature shows a significant variation with Zr content and reaches maximum value at x= 0.75. As Zr content increases, the samples become more frequency dependent and sensitive to any frequency variation. The coupling factor decrease by increasing Zr content from (0.64 to 0.92). Our nano composite BaZr_xTi_{1-x}O₃ compares to the published data has a high quality for electromechanical K_p in technological applications.

Author Contributions: M. Mostafa: Investigation, Visualization, Original Draft Preparation, Writing - Review and Editing. Aseel. M Altarawneh: Investigation, Formal Analysis, Visualization, Writing, Enas A Arrasheed: Investigation, Data Analysis, Visualization, R Ghazy: Visualization, Writing - Original Draft Preparation, Review and Editing, OM Hemed: Investigation, Visualization, Writing—Original Draft Preparation, Supervision and AMA Henaish: Resources, Visualization, Writing—Review and Editing. All authors have read and agreed to the published version of the manuscript.

Funding: All Authors declare that they have no funding sources for this research.

Data Availability Statement: The data that support the findings of this study are available on request from the corresponding author.

Conflicts of Interest: The authors declare no conflict of interest.

References:

- [1] Mallick J, Manglam M K, Pradhan L K, et al. Electrocaloric effect and temperature dependent scaling behaviour of dynamic ferroelectric hysteresis studies on modified BTO. *Journal of Physics and Chemistry of Solids [Internet]* **169**, p110844, 2022. Available from: <https://doi.org/10.1016/j.jpcs.1.10844>, 2022.
- [2] Zhao B, Zhang L, Zhen D, et al. A tailored double perovskite nanofiber catalyst enables ultrafast oxygen evolution. *Nature Communications* **8**, p 1–9, 2017.
- [3] Kushwaha H S, Madhar N A, Ilahi B, et al. Efficient Solar Energy Conversion Using $\text{CaCu}_3\text{Ti}_4\text{O}_{12}$ Photoanode for Photocatalysis and Photoelectrocatalysis. *Scientific Reports*. **6**, p1–10, 2016.
- [4] Rhouma F I H, Dhahri A, Dhahri J, et al. Dielectric, modulus and impedance analysis of lead-free ceramics $\text{Ba}_{0.8}\text{La}_{0.133}\text{Ti}_{1-x}\text{Sn}_x\text{O}_3$ ($x=0.15$ and 0.2). *Applied Physics A: Materials Science and Processing*. **108**, p593–600, 2012.
- [5] Sangwan K M, Ahlawat N, Kundu R S, et al. Structural, dielectric and ferroelectric properties of substituted BaZrTiO_3 lead-free ceramics. *AIP Conference Proceedings*. **2115**, p 0–4. 2019.
- [6] Ohara Y, Koumoto K, Yanagida H. Barium Titanate Ceramics with High Piezoelectricity Fabricated from Fibrous Particles. *Journal of the American Ceramic Society*. **68**, C-108-C-109. 1985.
- [7] Zhang S W, Zhang H, Zhang B P, et al. Dielectric and piezoelectric properties of $(\text{Ba}_{0.95}\text{Ca}_{0.05})(\text{Ti}_{0.88}\text{Zr}_{0.12})\text{O}_3$ ceramics sintered in a protective atmosphere. *Journal of the European Ceramic Society*. **29**, p 3235–3242, 2009.
- [8] Rashwan G M, Ebnalwaleda A A, Gerges M K, et al. Preparation and characterization and dielectric properties of $(\text{Ba}_{0.95}\text{Ca}_{0.05})\text{TiO}_3$ ceramic material. *International Journal of Thin Film Science and Technology*. **10**, p 127–135, 2021.
- [9] Pradhan L K, Kar M. Scaling behavior of dynamic ferroelectric hysteresis for semiconductor-relaxor (0-3) type $\text{ZnO}-(\text{Bi}_{0.5}\text{Na}_{0.5})_{0.94}\text{Ba}_{0.06}\text{TiO}_3$ composite. *Journal of Applied Physics*. **127**, p 0–9, 2020.
- [10] Rayssi C, El Kossi S, Dhahri J, et al. Frequency and temperature-dependence of dielectric permittivity and electric modulus studies of the solid solution $\text{Ca}_{0.85}\text{Er}_{0.1}\text{Ti}_{1-x}\text{Co}_x\text{O}_3$ ($0 \leq x \leq 0.1$). *RSC Advances [Internet]*. **8**, p 17139–17150, 2018. Available from: <http://dx.doi.org/10.1039/C8RA00794B>.
- [11] Qi J Q, Liu B B, Tian H Y, et al. Dielectric properties of barium zirconate titanate (BZT) ceramics tailored by different donors for high voltage applications. *Solid State Sciences [Internet]*. **14**, p 1520–1524, 2012. Available from: <http://dx.doi.org/10.1016/j.solidstatesciences.08p009>, 2012.
- [12] Urmi S A, Sumona H J, Sultan S. Synthesis and characterization of structural and

electrical properties of Zirconium doped Barium Titanate ceramics. **3**, p 8–11, 2022.

[13] Sangwan K M, Ahlawat N, Kundu R S, et al. Improved dielectric and ferroelectric properties of Mn doped barium zirconium titanate (BZT) ceramics for energy storage applications. *Journal of Physics and Chemistry of Solids* [Internet]. **117**, p 158–166, 2018. Available from: <https://doi.org/10.1016/j.jpcs.2018.01.051>.

[14] Nakashima K, Fujii I, Wada S. Preparation of BaZrO₃ nanocrystals at low temperature. *Key Engineering Materials*. **582** p 165–168, 2014.

[15] Potdar H S, Deshpande S B, Godbole P F, et al. Synthesis of microcrystalline bazro3 via molecular precursor route. *Journal of Materials Research*. **8** p 948–950, 1993.

[16] Charoonsuk P, Baitahe R, Vittayakorn W, et al. Synthesis of monodispersed perovskite barium zirconate (BaZrO₃) by the sonochemical method. *Ferroelectrics*. **453**, p 54–61, 2013.

[17] Li W, Xu Z, Chu R, et al. Structure and electrical properties of BaTiO₃ prepared by sol-gel process. *Journal of Alloys and Compounds*. **482**, p 137–140, 2009.

[18] Kaviani R, Saidi A. Sol-gel derived BaTiO₃ nanopowders. *Journal of Alloys and Compounds*.: **468**, p 528–532, 2009.

[19] Xu H, Gao L. Hydrothermal synthesis of high-purity BaTiO₃ powders: Control of powder phase and size, sintering density, and dielectric properties. *Materials Letters*. **58**, p 1582–1586, 2004.

[20] Yadav S, Chandra M, Rawat R, et al. Structural correlations in the enhancement of ferroelectric property of Sr doped BaTiO₃. *Journal of Physics Condensed Matter*. **32** (44), 2020.

[21] Mahesh M L V, Bhanu Prasad V V., James A R. Enhanced dielectric and ferroelectric properties of lead-free Ba(Zr 0.15Ti0.85)O₃ ceramics compacted by cold isostatic pressing. *Journal of Alloys and Compounds* [Internet]. **611**, p 43–49, 2014. Available from: <http://dx.doi.org/10.1016/j.jallcom.05.p098>. 2014.

[22] Jamil N H J, Izzuddin I, Zainuddin Z, et al. Microstructural studies of nanocrystalline barium zirconium titanate (BZT) for piezoelectric applications. *AIP Conference Proceedings*. 1678. 2015.

[23] Gaikwad S K, Ghodekar V G, Ramdasi O A, et al. Effect of Zr⁴⁺ substitution on ferroelectric and dielectric properties of BaTiO₃ ceramics. *AIP Conference Proceedings*. **1731** p 4–7, 2016.

[24] Badapanda T, Sarangi S, Behera B, et al. Structural refinement, optical and ferroelectric properties of microcrystalline Ba(Zr0.05Ti0.95)O₃ perovskite. *Current Applied Physics* [Internet]. **14**, p 708–715, 2014. Available from:

<http://dx.doi.org/10.1016/j.cap.2014.02.015>.

[25] Henaish A M A, Salem B I, Meaz T M, et al. Synthesize, characterization, dielectric, linear and nonlinear optical properties of Ni–Al Ferrite/PANI nanocomposite film. *Optical Materials*. **19**, p,111397, 2021.

[26] Chakrabarti N, Maiti H S. Chemical synthesis of barium zirconate titanate powder by an autocombustion technique. *Journal of Materials Chemistry*. **6**, p 1169–1173, 1996.

[27] Aktaş P S. Structural investigation of barium zirconium titanate Ba(Zr_{0.5}Ti_{0.5})O₃ particles synthesized by high energy ball milling process. *Journal of Chemical Sciences*. **132**, p 3–10, 2020.

[28] Hemeda O M, Eid M E A, Sharshar T, et al. Synthesis of nanometer-sized PbZr_xTi_{1-x}O₃ for gamma-ray attenuation. *Journal of Physics and Chemistry of Solids [Internet]*. **148**, p 109688, 2021, Available from: <https://doi.org/10.1016/j.jpcs.2020.109688>.

[29] Thananatthanachon T. Synthesis and Characterization of a Perovskite Barium Zirconate (BaZrO₃): An Experiment for an Advanced Inorganic Chemistry Laboratory. *Journal of Chemical Education*. **93**, p 1120–1123, 2016.

[30] Salem M M eta. Investigation of the structure and dielectric properties of doped barium titanates. **14**, p 3335–3345, 2024.

[31] Singh H H, Sharma A D, Sharma H B. Dielectric And Electrical Properties Of Barium Zirconate Titanate Ceramics. **5**, p 178–184, 2017.

[32] Pinjari R K, Aldar B A. Structural and Electrical Analysis of Strontium Substituted Barium Titanate. **3**, p 209–213, 2014. Available from: www.ijert.org.

[33] Kang W, Zheng Z, Li Y, et al. Effect of doping Gd₂O₃ on dielectric and piezoelectric properties of BaZr_{0.1}Ti_{0.9}O₃ ceramics by sol–gel method. *Journal of Materials Science: Materials in Electronics [Internet]*. **30** p 2743–2749, 2019. Available from: <http://dx.doi.org/10.1007/s10854-018-0550-7>.

[34] Kimura T, Dong Q, Yin S, et al. Synthesis and piezoelectric properties of Li-doped BaTiO₃ by a solvothermal approach. *Journal of the European Ceramic Society [Internet]*. **33**, p 1009–1015, 2013. Available from: <http://dx.doi.org/10.1016/j.jeurceramsoc>. **11**, p 007, 2012.

[35] Yang W G, Zhang B P, Ma N, et al. High piezoelectric properties of BaTiO_{3-x}LiF ceramics sintered at low temperatures. *Journal of the European Ceramic Society*. **32**, p 899–904, 2012.

[36] Tian Y, Wei L, Chao X, et al. Phase transition behavior and large piezoelectricity near the morphotropic phase boundary of lead-free (Ba_{0.85}Ca_{0.15})(Zr_{0.1}Ti_{0.9})O₃ ceramics. *Journal of the American Ceramic Society*. **96**, p 496–502, 2013.

- [37] Wu J, Xiao D, Wu W, et al. Composition and poling condition-induced electrical behavior of $(\text{Ba}_{0.85}\text{Ca}_{0.15})(\text{Ti}_{1-x}\text{Zr}_x)\text{O}_3$ lead-free piezoelectric ceramics. *Journal of the European Ceramic Society* [Internet]. **32**, p 891–898, 2012. Available from: <http://dx.doi.org/10.1016/j.jeurceramsoc>. **11**, p 003. 2011.
- [38] Acosta M, Novak N, Rojas V, et al. BaTiO₃-based piezoelectrics: Fundamentals, current status, and perspectives. *Applied Physics Reviews*. **4**, p 4, 2017.
- [39] Vo Thanh Tung, Nguyen Trong Tinh, Nguyen Hoang Yen DAT. Evaluation of Electromechanical Coupling Factor for Piezoelectric Materials Using Finite Element Modeling. *International Journal of Materials and Chemistry*. **3**, p 59–63, 2013.
- [40] Tuan D A, Tinh N T, Tung V T, et al. Ferroelectric and piezoelectric properties of lead-free BCT-xBZT solid solutions. *Materials Transactions*. **56**, p 1370–1373, 2015.